

Design optimization of a lightweight secondary mirror assembly for a 1-m class ground telescope for satellite laser ranging

Jaehyun Lee, Kisoo Park, Eui Seung Son, Suseong Jeong, Do-Won Kim, Han-Gyol Oh, Pilseong Kang & Hyug-Gyo Rhee

To cite this article: Jaehyun Lee, Kisoo Park, Eui Seung Son, Suseong Jeong, Do-Won Kim, Han-Gyol Oh, Pilseong Kang & Hyug-Gyo Rhee (2025) Design optimization of a lightweight secondary mirror assembly for a 1-m class ground telescope for satellite laser ranging, International Journal of Optomechatronics, 19:1, 2467152, DOI: [10.1080/15599612.2025.2467152](https://doi.org/10.1080/15599612.2025.2467152)

To link to this article: <https://doi.org/10.1080/15599612.2025.2467152>



© 2025 The Author(s). Published with license by Taylor & Francis Group, LLC



View supplementary material [↗](#)



Published online: 25 Feb 2025.



Submit your article to this journal [↗](#)



Article views: 76






View related articles [↗](#)



View Crossmark data [↗](#)

Design optimization of a lightweight secondary mirror assembly for a 1-m class ground telescope for satellite laser ranging

Jaehyun Lee^a , Kisoo Park^b, Eui Seung Son^b, Suseong Jeong^c, Do-Won Kim^a, Han-Gyol Oh^{a,d}, Pilseong Kang^a , and Hyug-Gyo Rhee^{a,d} 

^aKorea Research Institute of Standards and Science (KRISS), Daejeon, Republic of Korea; ^bDefense Rapid Acquisition Technology Research Institute, Seoul, Korea; ^cHanwha Systems, Seongnam, Korea; ^dDepartment of Precision Measurement, University of Science and Technology, Daejeon, Republic of Korea

ABSTRACT

Large-sized ground telescopes have been developed to meet the high demands for opto-mechanical imaging systems in space and military applications. In line with these advancements, we developed a 1-m class ground telescope for astronomical imaging and satellite laser ranging (SLR). In a ground telescope, mirror deflection is mainly induced by gravity and temperature change. In particular, the gravity vector varies depending on the pointing direction of a telescope, so the surface deformations of the mirrors due to self-gravity need to be managed in different observation directions. This study introduces a mechanical design for an optical tube assembly (OTA) and suggests an optimized design for the secondary mirror (M2) assembly. For a kinematic positioning of the M2, its lightweight was achieved based on the partially open-back structure with hexagonal pocket cells. Then, we optimized the flexure mount design with a bipod structure to minimize the surface errors (SFEs) of the M2 in both the horizontal and vertical pointing directions. Additionally, we simulated the deflections of the primary mirror (M1) and M2 assemblies when installed on the telescope. Based on our design, the M2 was fabricated and processed, and we demonstrated its assembly process and surface quality test.


KEYWORDS

Design optimization; optical telescope; mirror lightweight; optical alignment; satellite laser ranging

1. Introduction

Recently, large-sized ground and space telescopes have been developed in the fields of astronomy and national defense. The key feature of space telescopes is that they are not affected by the atmosphere. Consequently, many space telescopes have been developed despite high launching costs and stringent design requirements. Space telescopes require a lightweight mirror when considering the satellite payload. Ground telescopes are more flexible and cost-effective, making them larger than space telescopes.^[1,2] However, they require adaptive optics (AO) systems to compensate for image distortion caused by atmospheric turbulence. A deformable mirror of the AO system for compensating a wavefront error is located on the external part of the

CONTACT Pilseong Kang  pskang@kriss.re.kr; Hyug-Gyo Rhee  hrhee@kriss.re.kr  Korea Research Institute of Standards and Science (KRISS), Daejeon, Republic of Korea.

 Supplemental data for this article can be accessed online at <https://doi.org/10.1080/15599612.2025.2467152>.

© 2025 The Author(s). Published with license by Taylor & Francis Group, LLC

This is an Open Access article distributed under the terms of the Creative Commons Attribution-NonCommercial License (<http://creativecommons.org/licenses/by-nc/4.0/>), which permits unrestricted non-commercial use, distribution, and reproduction in any medium, provided the original work is properly cited. The terms on which this article has been published allow the posting of the Accepted Manuscript in a repository by the author(s) or with their consent.

collimator,^[3,4] or a secondary mirror (M2) acts as a deformable mirror itself.^[5,6] Like the latter case, a lightweight mirror is required in a ground telescope considering the mass budget of a mechanical component.

Depending on their structures, lightweight designs are classified into an open-back, sandwich, and partially open-back type.^[7,8] The open-back type offers the highest lightweight ratio, and the sandwich type provides the highest stiffness-to-weight ratio using a back sheet plate. The partially open-back type is a variant of the sandwich type, in which cap holes are made on the back sheet plate. The advantages of this method are that the mirror is not divided, and the shear center can be adjusted by modifying the sizes of the cap holes. Lightweight pockets typically have a triangular, square, or hexagonal shape to maintain symmetry. Among them, the hexagonal structure is known to be the most robust to the quilting effect during mirror fabrication and deflection due to gravity.^[9] To reduce surface deformations, mirrors utilize flexure structures on their mounts. An elaborate flexure structure design is necessary because lightweight mirrors are more sensitive to environmental changes due to reduced stiffness. The positions of the flexure mounts are also carefully managed to align them on the shear centers in both the axial and lateral directions.^[10] The optimal designs of lightweight mirrors and flexure mounts have been demonstrated in previous studies for space applications.^[11–19] Notably, Kihm *et al.*^[14] optimized the 1-m size lightweighted mirror using a multi-objective genetic algorithm. Chen *et al.*^[16] optimized a lightweight structure and bipod flexure mount for a 550-mm primary mirror. The design of a mirror assembly with a lightweight mirror for a ground telescope has also been reported in prior studies.^[1,2,20,21] However, to the best of our knowledge, the design optimization of a lightweight mirror and flexure mount and the analysis for mirror deflection of the ground telescope have not been demonstrated in detail until now. Also, the results for the mirror fabrication, assembling and surface measurements are not introduced comprehensively in previous works.

This study introduces the design of a 1-m class ground telescope. It consists of an optical part, including a primary mirror (M1), M2, and third mirror (M3) assemblies and mechanical frames that supports these components. In a ground telescope, mirror deflection is mainly induced by self-gravity and temperature change. In particular, the gravity vector depends on the pointing direction of the telescope, and the surface errors (SFEs) of the mirrors change accordingly. In our case, the mirror assemblies should satisfy the SFE budgets for self-gravity (at all elevation angles) and temperature variation (from -10°C to 40°C). Additionally, mirror deflection increases due to the structural deformation of an optical tube assembly (OTA). Mechanical frames are designed to minimize its gravitational deformation considering design constraints on mass, size, and stiffness. To compensate the deflections of the mirrors induced by gravity and temperature change and by the error of mechanical assembly, a posture control device is required on the OTA. We adopted a hexapod on the back of the M2 assembly to align it with respect to the M1 in real time. To satisfy the mass budget of the hexapod, we designed a lightweight M2 having a hexagonal structure with a partially open-back type to effectively achieve the lightweight of M2. Then, we applied a flexure mount with a bipod structure. The designs for the lightweight M2 and flexure mount are optimized to minimize the SFEs in both the vertical and horizontal pointing directions.

Meanwhile, satellite laser ranging (SLR) is one of the promising applications of ground telescopes.^[22–33] SLR telescopes usually have the aperture sizes of several tens of centimeters and 1-m class telescopes are also often utilized for SLR.^[32,33] SLR is utilized in different research fields, including Earth orbiting satellites,^[26] ground-to-satellite communications,^[27,28] geodesy,^[29] and space debris.^[30,31] In a SLR telescope, key features for an accurate ranging are light-gathering power, time gating, beam divergence angle, and angular resolution. Our telescope aims at both astronomical imaging and SLR, and therefore, it requires strict requirements for both the optical and mechanical designs.

In this study, we present the results for mirror processing, assembling, and surface quality tests for the M2 based on our optimized designs. In Chapter 2, we introduce the design of the OTA including the configuration of the M2 assembly and its design requirements. Chapter 3 demonstrates the shape optimization process of the lightweight M2 with hexagonal pocket cells. In Chapter 4, we optimize the sizes of the M2 with a partially-open back structure. Chapter 5 introduces the optimization process of the flexure mount design with a bipod structure. The 3D model of the OTA was prepared using Ansys SpaceClaim and finite element analysis was performed using Ansys Mechanical to calculate the surface deformation of the M2. Using MATLAB, the SFE was expressed by Zernike polynomials, and the optimized design point was derived, which provides the lowest SFE. The whole optimization processes simultaneously consider the mass budget, allowable bond stress, mirror processability, and thermally-induced SFE. In Chapter 6, we simulated the deflection of M1 and M2 after installing them onto the OTA in different pointing directions. Finally, we demonstrate the results of the fabrication, assembling, and surface quality tests for the M2 assembly in Chapter 7.

2. Designs of the optical tube assembly and second mirror assembly

2.1. Telescope design

Figure 1 shows the overall configuration of the optical tube assembly (OTA).^[34] We used the A-shaped Serrurier scheme for the OTA to reduce the structural deformation. The sizes of the OTA are approximately 4 m in height, 2 m in width, and 2 m in depth. As shown in Figure 1(a), the OTA consists of a bottom, top, and middle section. The bottom frame holds the primary mirror (M1) assembly, with an aperture size of approximately 1.5 m. The top frame holds the secondary mirror (M2) assembly consisting of the M2, supporting mounts, and a hexapod. The clear aperture size of the M2 is approximately 0.3 m and the spider vane connects the M2 assembly to the OTA frame. The top and bottom frames have a dodecagonal shape and the four bipod trusses connect them to the middle frame. The tracking mount, which controls the observation angle of the OTA, is connected with the OTA at the interfaces of the middle frame shown in Figure 1(c). The allowed budgets of the total mass and rotational inertia momentum for the OTA are determined by the performance of the tracking mount and the shear center of the OTA should be positioned at its rotational axis. Within those design constraints, the parametric studies on the OTA sizes were performed to reduce its structural deformation due to self-gravity.^[34] The flat

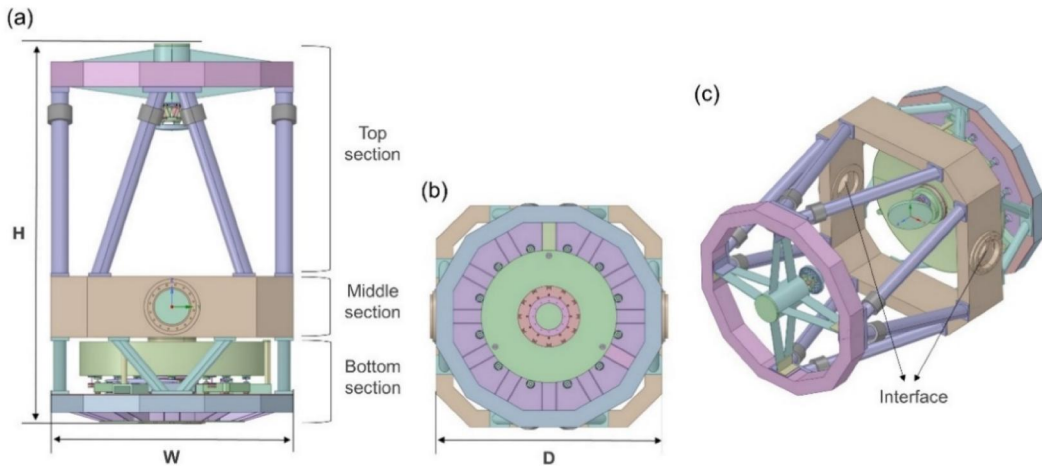


Figure 1. Overall configuration of the optical tube assembly (OTA). (a) Front view, (b) Bottom view, (c) Isometric view. W: width, H: height, D: depth.

third mirror (M3) is located at the upper part of the primary mirror, inclined at 45° to deliver a collimated beam to the coudé pass. The design optimization for the M3 assembly was performed to minimize its SFE.^[35] The SFEs of the mirrors were simulated in advance, and the hexapod (Bora, Symetrie Inc.)^[36] will automatically adjust the position of the M2.

2.2. Secondary mirror assembly design

Figure 2(a) introduces the optical path of the OTA for astronomical imaging. M1 and M2 collect and collimate the beam, and M3 transfers the collimated beam to the observation facility. For SLR, a high-power laser is transmitted to the atmosphere in a reverse manner. Table 1 presents the design parameters for the M2 assembly. The M2 is a convex parabolic mirror with a radius of curvature of 900 mm. Its clear aperture and center thickness are 300 and 50 mm, respectively. Its material is astrosital, and the mass of the bare mirror is 8 kg. Figure 2(b) shows the overall configuration of the M2 assembly, directed in the horizontal direction. The assembly consists of the M2, flexure mount, adapter plate, and hexapod. The three flexure mounts are bonded to the M2 at the symmetrically-positioned mounting pockets. Table 2 introduces the budgets of the masses and SFEs for the M2 assembly. The mass budget of the hexapod is 5 kg. Based on the basic model design, we set the mass budgets of the M2 and its mount as 3.6 kg and 1.4 kg. The corresponding lightweight ratio is approximately 60%. The RMS values of the SFE budgets are 7.5 nm for the M2 and 30 nm for the three mirrors (M1, M2, and M3). The SFE budgets are determined by considering the imaging resolution. The flexure mount and adapter plate are made of invar36 material to reduce thermally-induced SFE. Table 3 represents the material properties utilized in the study.

3. Optimization for the lightweight pockets

Figure 3 shows the lightweight mirror design with the hexagonal-shaped pocket cells. The mounting pockets are arranged symmetrically and provide space for bonding the flexure mounts. In this study, the SFEs were examined for both directions: the vertical pointing direction (SFE-z), where the telescope directs at 90° in elevation and the horizontal pointing direction (SFE-y), where the telescope directs at 0° in elevation. Before realizing the lightweight mirror design, we first determined the shape of the mounting structure. Considering the SFE-z and SFE-y, the plate-mount type was chosen for the mounting scheme (Figure S1). A detailed study is provided in the

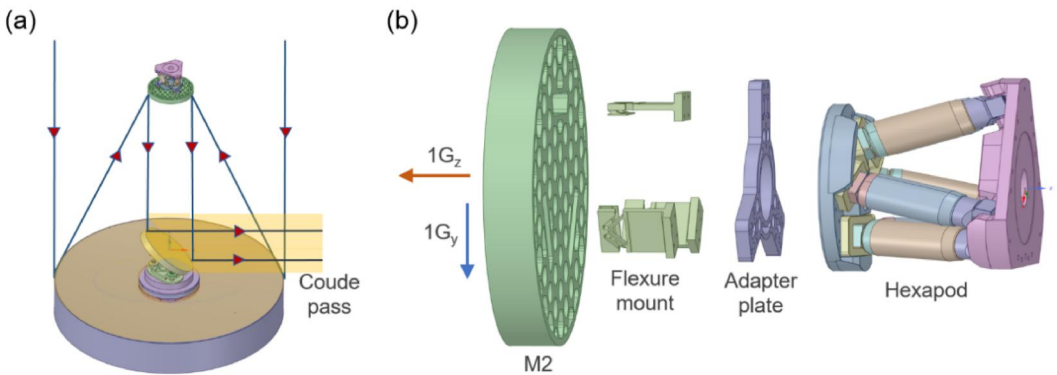


Figure 2. Configurations for optical path and secondary mirror (M2) assembly. (a) Beam path of optical tube assembly. M1 and M2 collimates the beam and M3 transfers it to coudé pass. (b). Configuration of the M2 assembly. It consists of the M2, flexure mount, adapter plate and hexapod. The red and blue arrows represent the direction of gravity in the vertical and horizontal directions, respectively.

Table 1. Design parameters of the M2.

| Type | Radius of curvature | Clear aperture | Center thickness | Bezel size | Material | Mass of bare mirror |
|-----------------|---------------------|----------------|------------------|------------|------------|---------------------|
| Convex parabola | 900 mm | 300 mm | 50 mm | 2 mm | Astrosital | 8 kg |

Table 2. Budgets for the masses and surface errors.

| Mass budget (M2 assembly) | Mass budget (Mirror) | Mass budget (Mirror mount) | Surface error (SFE) budget* | Total SFE budget of three mirrors ^a |
|---------------------------|----------------------|----------------------------|-----------------------------|--|
| 5.0 kg | 3.6 kg | 1.4 kg | 7.5 nm in RMS | 30 nm in RMS |

RMS: Root Mean Square.

^aBoth in the z- and y-axis.

Table 3. Material properties.

| Material type | Young's Modulus (GPa) | Poisson ratio | Density (kg/mm ³) | Thermal expansion coefficients (mm/mm/K) |
|---------------|-----------------------|---------------|-------------------------------|--|
| Astrosital | 92.0 | 0.28 | $2.46 \cdot 10^{-6}$ | $1.50 \cdot 10^{-7}$ |
| EC2216 | 0.69 | 0.43 | $1.32 \cdot 10^{-6}$ | $1.02 \cdot 10^{-4}$ |
| Invar36 | 141.0 | 0.26 | $8.05 \cdot 10^{-6}$ | $1.26 \cdot 10^{-6}$ |

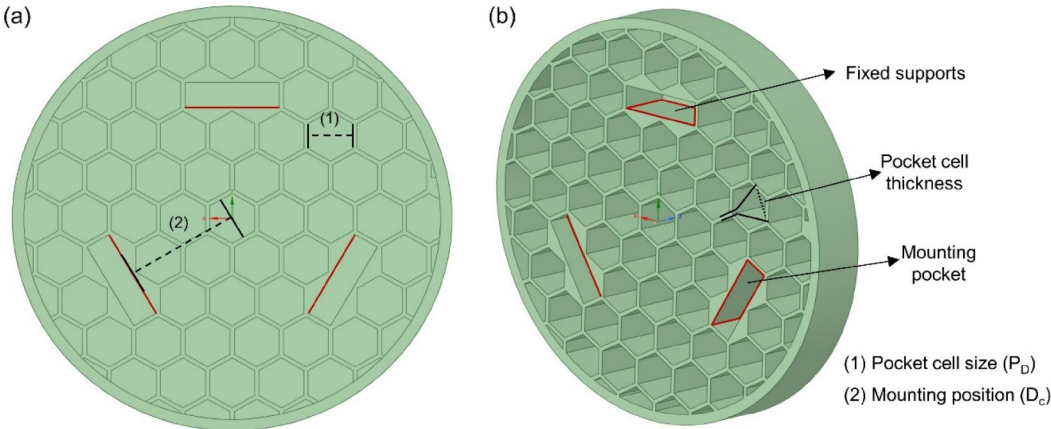


Figure 3. Lightweight mirror design with hexagonal pocket cells. (a) Front view, (b) Isometric view. The mounting positions are marked as red lines. The positions of the fixed supports are identical to that of the mounting positions. The design variables, pocket cell size (P_D) and mounting position (D_c) are shown. The mounting position denotes the distance between the mounting pocket and the center of the mirror.

supplementary section. Our topology optimization covers determining the shapes and sizes of lightweight pocket cells and mounting pockets. We adopted hexagonal pocket cells considering the robustness against quilting effect. Additionally, we determined the mounting pockets as a cuboid shape considering the mounting structure. We then optimized the size of the pocket cells and the corresponding position of the mounting pockets. This step is crucial for minimizing the SFE-z as the size of the pocket cells determines the position of the shear center. The design range of the pocket cell size was from 28 to 38 mm, and we determined the mounting position that minimizes the SFEs for each pocket cell size. The design steps for the pocket cell size and mounting position are 1 and 0.1 mm, respectively. Other design parameters, the cell wall thickness, outer rim thickness, and face sheet plate thickness, were initially set as 3, 7, and 7 mm, respectively. As shown in Equation (1), the required bonding area relates to the mirror mass and allowable bond stress.

$$A \geq \frac{M}{S} \quad (1)$$

Here, A , M , and S denote bonding area (mm^2), mirror mass (N), and allowable bond stress (N/mm^2), respectively. In our home-test, the allowable bond stress of EC2216 was found to be 6.2 MPa between the glass and Invar36 material.^[37] At this point, the safety factor covers the margin for the impact loads, mirror fabrication inaccuracies, and assembly misalignments. By considering the safety factor, we determined the minimum bonding area as 400 mm^2 . To have enough space for the bonding process, the sizes of the mounting pockets were set to be 60 mm in width and 25 mm in depth, marked with red lines in Figure 3. The optimization process for the pocket design is shown in Figure 4. The 3D model of the M2 was prepared using Ansys SpaceClaim, and finite element analysis was performed using Ansys Mechanical to derive the nodal deformations of the M2 surface. The surface deformation was manipulated in the MATLAB program. The tilt and defocus terms, which can be compensated by using a hexapod, were removed to calculate the SFE-z and SFE-y. We utilize the ISO-14999 indexing scheme to represent the Zernike polynomial.^[38,39] Finally, the optimal design point returns the minimal objective function (f), where E_z and E_y indicate the SFE-z and SFE-y, respectively. To cover the whole pointing directions of the OTA, we managed both the SFE-z and SFE-y equally. Therefore, we determined their weight coefficients of as 1.

$$f(E) = \sqrt{E_z^2 + E_y^2} \quad (2)$$

Figures 5(a) and (b) introduce the deformation of the M2 induced by self-gravity in the vertical pointing direction. The gray wireframe in Figure 5(b) shows the undeformed mirror shape. Its amplitudes of Zernike polynomials are represented in Figure 5(c). Due to the reduced stiffness, the defocus and trefoil terms are dominantly increased in the lightweight mirror. Figure 6 shows the SFE values of the bare mirror (blue dots) and the lightweight mirror (green dots) when the pocket cell size is 31 mm. In the case of the bare mirror, the SFE value has a minimal value of 1.78 nm with a mounting position of 82.8 mm. The lightweight mirror is 3.39 nm with a mounting position of 68.9 mm. The converged points are determined for each pocket cell size, and the corresponding SFE-z and mass of the M2 for each design are introduced in Table 4.

4. Size optimization of the lightweight design with a partially open back structure

Figure 7 shows the shape of the lightweight M2 with the hexagonal pocket cells. We adopted a partially open back scheme for the lightweight design, which a T-shape milling tool fabricated

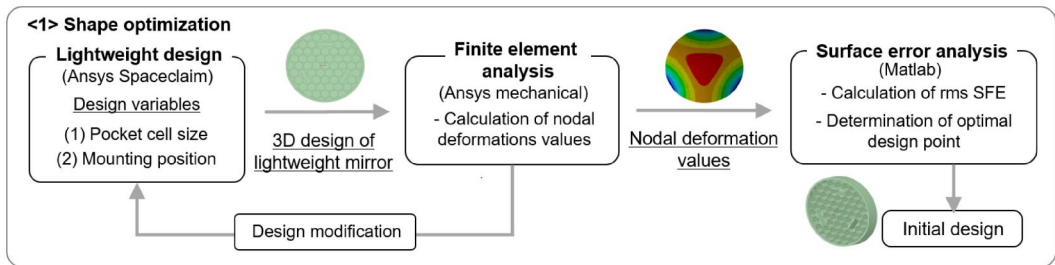


Figure 4. The shape optimization process of the lightweight design. The 3D model of the M2 was prepared using Ansys SpaceClaim. The nodal deformations of the M2 surface were calculated based on FEA simulation using Ansys Mechanical. Then, the coefficients of the Zernike polynomial were derived using MATLAB. The optimal point providing the lowest SFEs is determined in the optimization process. The determined shape was utilized as an initial design in the following size optimization process.

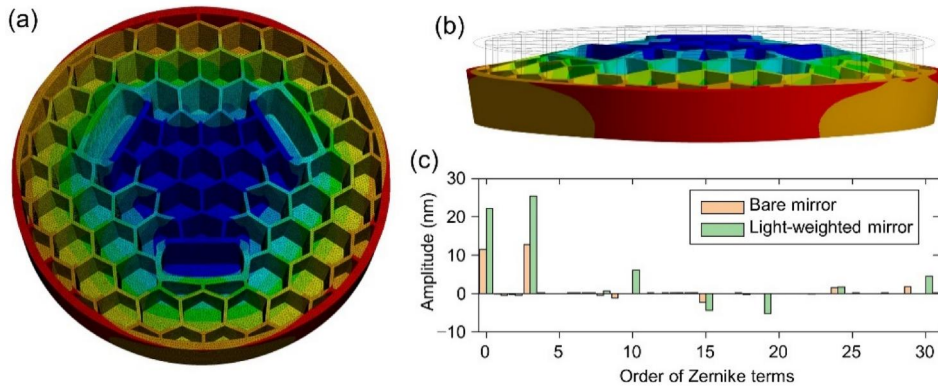


Figure 5. The surface deformation of the M2 in the vertical pointing direction when the pocket cell size is 30 mm. (a) Top view, (b) Side view, (c) Amplitudes of Zernike terms before (orange) and after lightweight (green). The bare mirror only has mounting pockets at the shear center.

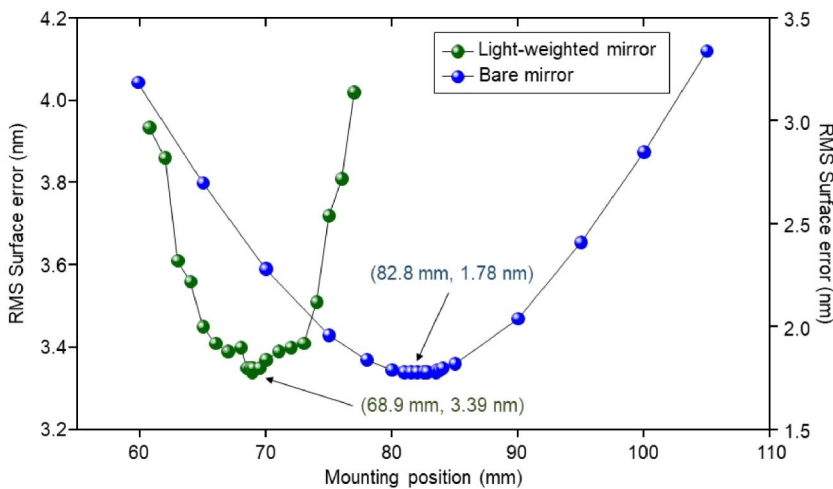


Figure 6. Optimal point of the mounting position. The RMS SFE-z in the vertical direction is 3.39 nm for the lightweight mirror when the pocket size is 31 mm.

Table 4. The surface errors (SFEs) in the vertical direction and masses of the M2 after shape optimization.

| Design point | 1 | 2 | 3 | 4 | 5 | 6 | 7 | 8 | 9 | 10 | 11 |
|------------------------|------|------|------|------|------|------|------|------|------|------|------|
| Cell size (mm) | 28 | 29 | 30 | 31 | 32 | 33 | 34 | 35 | 36 | 37 | 38 |
| Mounting position (mm) | 69.7 | 69.2 | 69.3 | 68.9 | 66.0 | 66.3 | 66.9 | 68.0 | 68.5 | 68.6 | 68.2 |
| SFE-z in RMS (nm) | 3.29 | 3.21 | 3.27 | 3.39 | 3.50 | 3.68 | 3.79 | 3.83 | 3.91 | 4.12 | 3.99 |
| Mass (kg) | 3.14 | 3.15 | 3.14 | 3.12 | 3.12 | 3.07 | 3.04 | 2.99 | 2.99 | 3.00 | 2.84 |

through the cap holes. The design variables include the thicknesses of the front and back sheet plate, outer rim, and rib, the diameter of the cap hole, and the round of the pocket cell. The size modifications of these variables lead to a slight shift in the shear center, increasing the value of the optimized SFE-z. Therefore, we re-optimized the mounting position (D_c) to minimize the value of the SFE-z. Table 5 introduces their design ranges and design steps. The ranges of the design variables are related to mirror manufacturability and mass budget. Their minimal values represent the limit of feasible mirror manufacturing, while their maximum values consider the mass budget of 3.6 kg. The general manufacturing tolerance is reflected in the design steps.

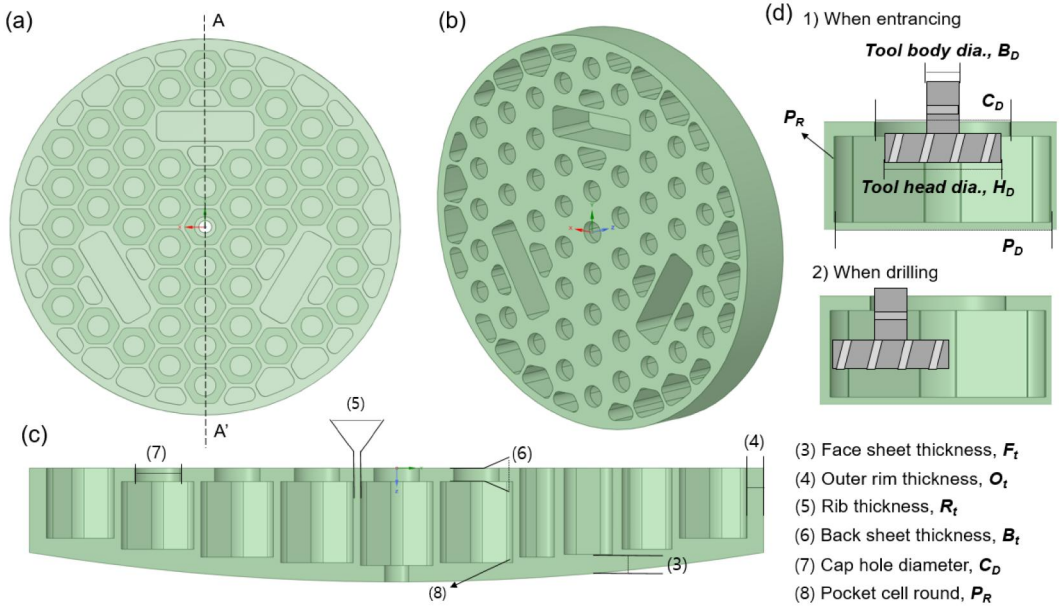


Figure 7. Lightweight mirror design. (a) Front view, (b) Isometric view, (c) Section view (A-A'). (d) The design requirements for the T-shaped milling tool when entrancing and drilling. The back sheet plate is introduced in the size optimization process. The design variables are the face sheet plate thickness (F_t), outer rim thickness (O_t), rib thickness (R_t), back sheet plate thickness (B_t), cap hole diameter (C_D), and pocket cell round (P_R). B_D and H_D denote the diameters of the T-shaped tool body and head, respectively.

Table 5. Parameters of the design variables for the size optimization.

| Design variable | Pocket cell Size | Mounting position | Face sheet thickness | Outer rim thickness |
|----------------------|------------------|----------------------|----------------------|---------------------|
| Initial design point | 31 | 68.9 | 7.0 | 7.0 |
| Design range | 28–38 | 60–80 | 7.0–11.0 | 7.0–14.0 |
| Design step | 1 | 0.1 | 0.1 | 0.1 |
| Optimal design point | 30 | 69.2 | 7.0 | 7.0 |
| Design variable | Rip thickness | Back sheet thickness | Cap hole diameter | Pocket cell round |
| Initial design point | 3.0 | 8.0 | 20.0 | 10.0 |
| Design range | 3.0–5.5 | 6.0–16.4 | 15.0–25.0 | 8.0–12.0 |
| Design step | 0.1 | 0.1 | 0.1 | 0.2 |
| Optimal design point | 3.0 | 6.2 | 22.4 | 8.8 |

All units are millimeters (mm). The initial design point represents the lightweight design of the shape optimization, and the optimal design point represents the lightweight design after the size optimization.

Additionally, the cap hole diameter, the round of the pocket cell, and pocket cell size should be controlled by considering the milling process with a T-shaped tool. In our fabrication shop, the restrictions of the design variables for the fabrication process were as follows.

$$\frac{C_D}{2} \geq \frac{H_D}{2} + 1 \quad (3)$$

$$\frac{C_D}{2} - \frac{B_D}{2} \geq \frac{P_D}{2} - \frac{H_D}{2} + 1 \quad (4)$$

$$P_R \geq H_D \quad (5)$$

Here, C_D , H_D , B_D , P_D , and P_R denote the cap hole diameter, tool head diameter, tool body diameter, pocket cell size, and round of the pocket cell, respectively. Equations (3) and (4) denote the conditions that the T-tool is away from the edge of the cap hole at least 1 mm when it entrances and drills, respectively. If we assume that B_D is 8 mm and P_R equals $H_D/2$, then Equations (6) and (7) are derived as below.

$$\frac{C_D}{2} \geq \frac{P_D}{2} - P_R + 5 \quad (6)$$

$$\frac{C_D}{2} \geq P_R + 1 \quad (7)$$

Considering these restrictions, we performed the size optimization as introduced in Figure 8. The procedure of the size optimization was the same as that of the shape optimization, and the initial M2 design was provided from the shape optimization. Here, we added a hole with a 10 mm diameter on the center of the M2 surface. Then, a flat mirror was attached to the back of the M2 to be parallel with the M2 surface. It will be utilized as a reference plane when aligning the optical path of the coude pass. The objective function (f) is the same as that in the shape optimization process (Equation (2)), where E_z and E_y indicate SFE-z and SFE-y, respectively (Equation (8)).

$$f(E) = \sqrt{E_z^2 + E_y^2} \quad (8)$$

Table 5 introduces the design points of the optimized lightweight structure. Figures 9(a) and (b) show its surface deformations in the vertical and horizontal pointing directions, respectively. After removing the tilt and defocus terms of the Zernike polynomial, the RMS values of SFE-z and SFE-y are 2.35 and 1.67 nm, respectively. Figure 9(c) shows the amplitudes of the Zernike terms before and after size optimization. A back sheet plate was introduced in the size optimization, resulting in increased stiffness. Consequently, the defocus term (3rd) and foil-terms (10th, 15th, 19th, 30th) are reduced noticeably after the size optimization.

5. Optimization of the flexure mount design

In this section, we optimize the design of the flexure mount made with the Invar36 material. Figure 10 shows the 3D design of the flexure mount and its design variables. As shown in Figure 10(c), the flexure mount consists of a head, body, and leg part with a bipod structure. The upper side of the head part is connected to the adapter plate, and the plate of the leg part attaches to

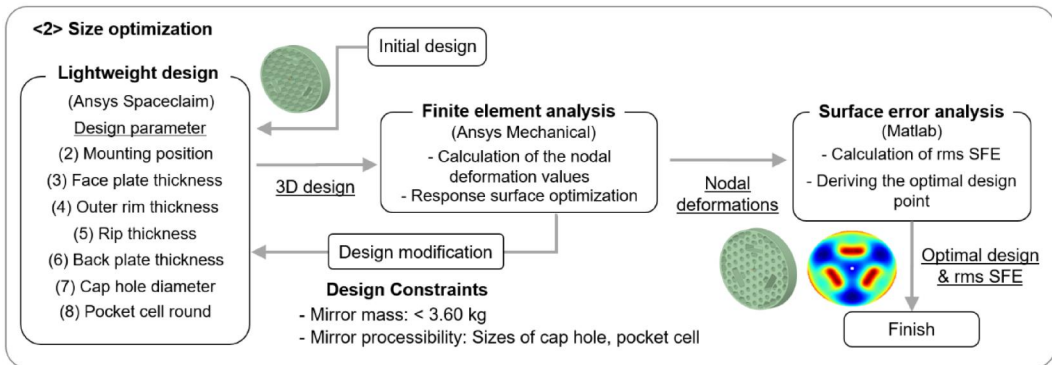


Figure 8. The size optimization process for the lightweight mirror structure. In each pocket cell size, the other design variables were optimized by following the same process explained in Figure 4. Here, the design constraints are the mirror mass and the sizes of the cap hole, pocket cell diameter, and the round of the pocket cell.

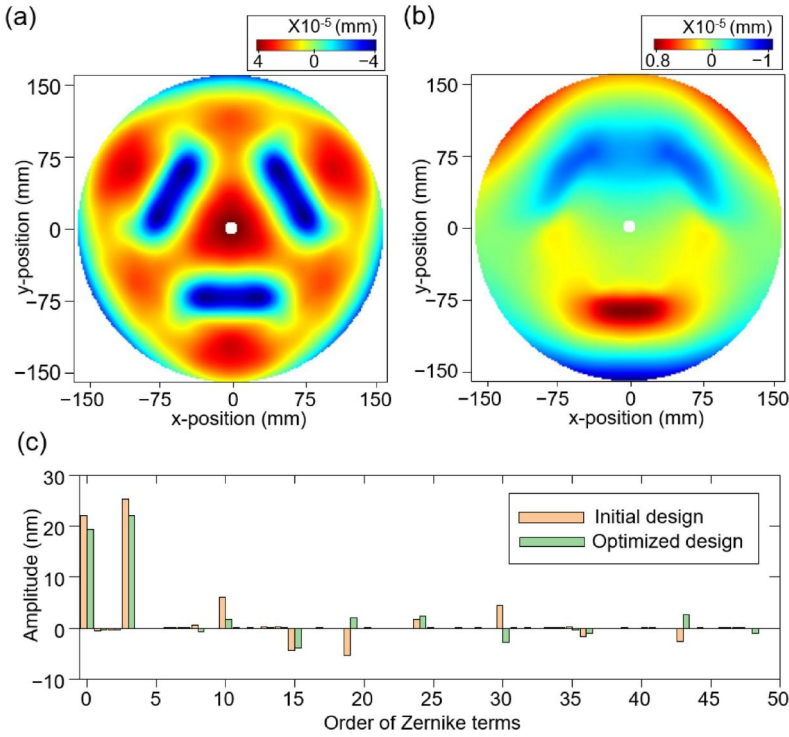


Figure 9. The surface deformations after the size optimization. (a) The SFE-z in the horizontal direction, (b) The SFE-y in the vertical direction, (c) The amplitudes of the Zernike terms after the shape optimization (red) and size optimization (green).

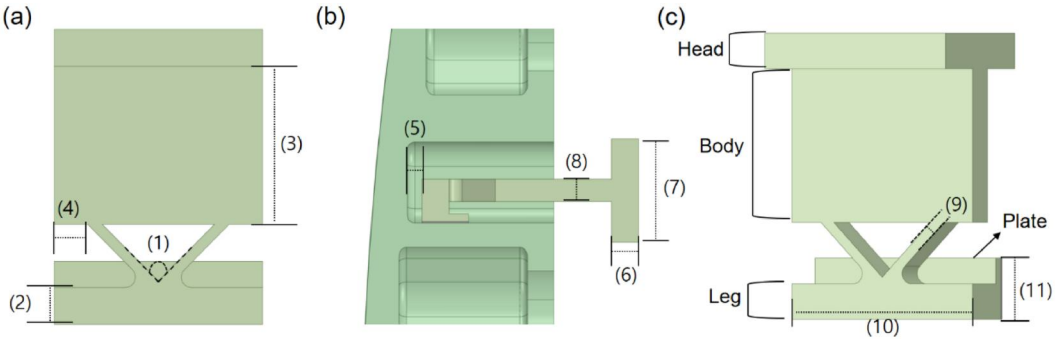


Figure 10. The designs of the flexure mount. (a) The front view, (b) The side view in the horizontal direction, and (c) The isometric view. The design variables are as follows: (1) Bipod angle, (2) Leg height, (3) Body height, (4) Lateral bipod-position, (5) Axial flexure-position, (6) Head height, (7) Head depth, (8) Body depth, (9) Bipod thickness, (10) Plate length, (11) Plate height.

the mounting pockets of the M2. First, we optimized the design variables that determine the pivot point of the bipod structure, including the bipod angle and thickness, leg height, body height, lateral bipod-position, and axial flexure-position shown in Figures 10(a) and (b). The arrangement of the pivot point at the shear center in the horizontal direction minimizes the SFE-y of the M2. Figure 11 shows the optimization process for the flexure mount design. After performing the pivot point optimization, we optimized the sizes of the other design variables: head height and depth, body depth, and plate length and height. In this process, we used the design constraints for the total mass, assembly condition, and total height. The sizes of the head part were determined by considering the assembly with the adapter plate, and the allowable bond stress and

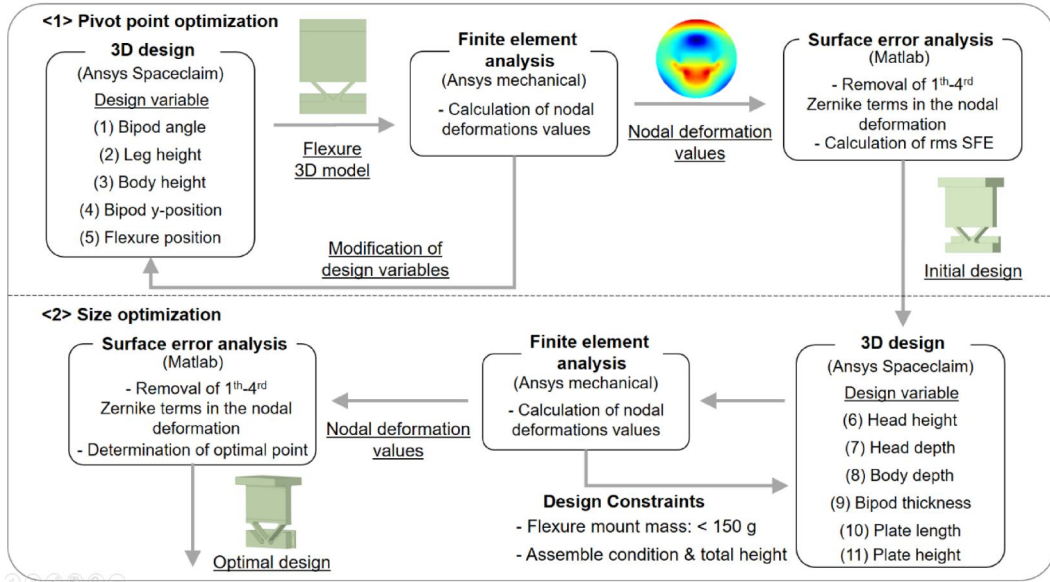


Figure 11. Optimization process for the flexure mount. The design variables for the bipod angle and thickness, leg height, body height, lateral bipod-position, and axial flexure-position were optimized to determine the pivot point. Then, size optimization was performed for the other design variables: head height, head depth, body depth, plate length, and plate height. The design constraints were the mass of the flexure mount, the sizes for assembly, and the total height of the flexure mount.

Table 6. Parameters for the design variables and the optimal design point for the flexure mount.

| Design variable (unit) | Bipod angle (degree) | Leg height (mm) | Bipod y-position (mm) | Flexure position (mm) |
|------------------------|----------------------|----------------------|-----------------------|-----------------------|
| Initial design point | 90 | 6 | 6 | 7.5 |
| Design range | 90–110 | 4–8 | 2–6 | 2–12 |
| Design step | 0.2 | 0.1 | 0.1 | 0.1 |
| Optimal design point | 100 | 3.0 | 5.0 | 2.4 |
| Design variable (unit) | Body depth (mm) | Bipod thickness (mm) | Plate length (mm) | Plate height (mm) |
| Initial design point | 6.0 | 2.0 | 40.0 | 10.0 |
| Design range | 4–6 | 1–2 | 40–45 | 10–15 |
| Design step | 0.1 | 0.1 | 0.1 | 0.1 |
| Optimal design point | 5.6 | 1.6 | 45.0 | 15.0 |

thermally-induced SFE restricted the sizes of the plate. Additionally, the total length of the flexure mount was determined by considering the distance between the M2 surface and the M1 surface.

After considering all the design constraints, we derived the optimal design for the flexure mount. The design variables for the flexure mount and optimal design point are presented in Table 6. The objective function (f) is identical to the previous optimization processes, the SFE-z and SFE-y RSS values. Before the optimization, the initial SFE-z and SFE-y were 4.13 and 5.7 nm, respectively. Figures 12(a) and (b) show the surface deformations of the optimized design in the vertical and horizontal directions, respectively. After the optimization, the RMS values for the SFE-z and SFE-y are 4.21 and 2.16 nm, respectively. The variation of the SFE-z is negligible compared to that of SFE-y. At the same time, we analyzed the surface deformation due to temperature change. The thermally-induced SFE was monitored during the entire optimization processes and we identified that it is dominantly affected by the sizes of the bonding area. As shown in Figure 12(c), the RMS value for the SFE is 0.28 nm for a temperature change of 5 K, satisfying the SFE budget.

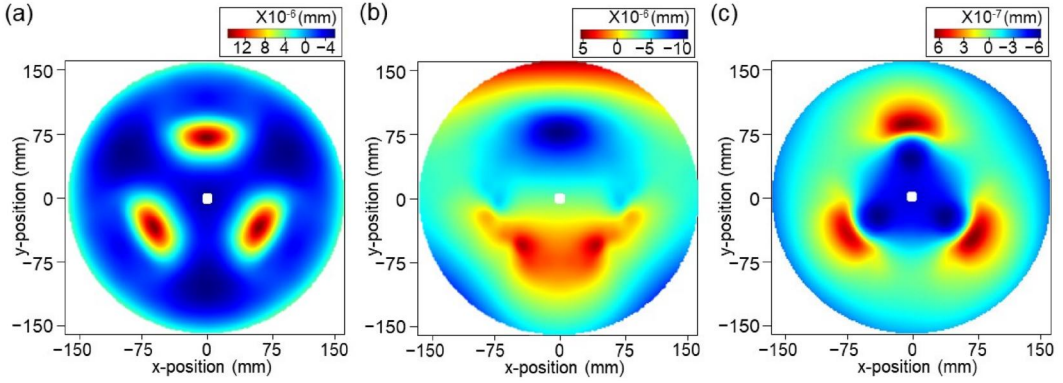


Figure 12. The surface deformations after the size optimization. (a) The surface deformation in the vertical pointing direction, (b) The surface deformation in the horizontal pointing direction. (c) The surface deformation for a temperature change of 5 K. The low terms of the Zernike polynomial are removed in the MATLAB program.

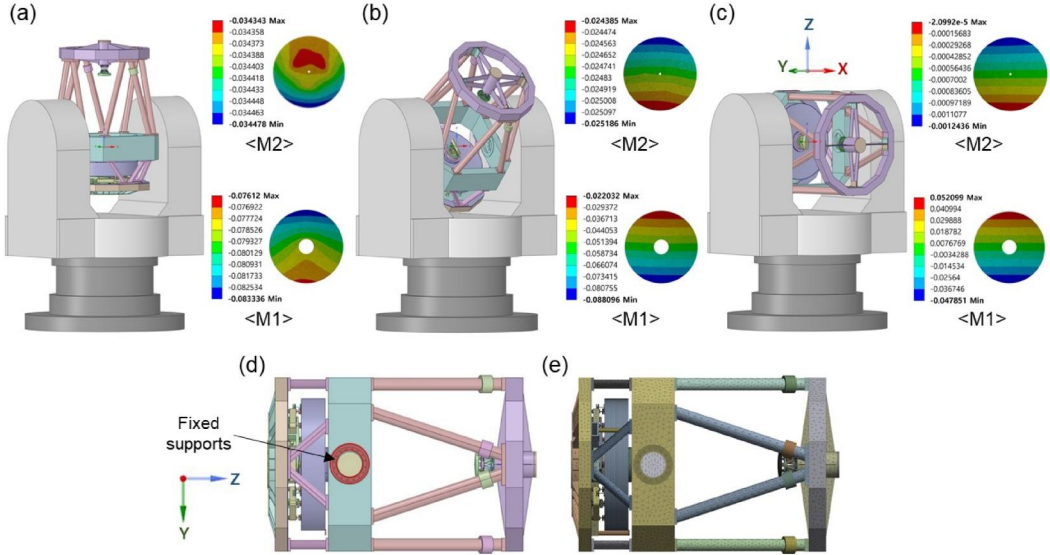


Figure 13. The surface deformations of the M1 and M2 due to the deflection of the OTA. (a) Surface deformations in the vertical direction, (b) Surface deformations in the observation angle of 45°, and (c) Surface deformations in the horizontal direction. The coordinate system is represented in (c). In the horizontal direction, the M2 surface directs the +y direction and the M3 surface directs the +x direction, (d) The fixed supports positioned at the interfaces of the middle frame with the tracking mount, (e) The generated mesh of the OTA in Ansys mechanical. The number of nodes is 6,549,409. All contact conditions in the simulation are set as bonded contact.

6. Analysis of mirror deflection from the deformation of the OTA

Until now, we optimized the deflection of the M2 assembly induced by self-gravity and temperature change. After installing the mirror assembly on the OTA, the mirror deflection increases due to the structural deformation of the OTA. It affects the M1 and M2 misalignment, generating imaging distortion of the collimated beam. Moreover, it modifies the optical path of the laser beam, inducing inaccuracies in the SLR. Therefore, we analyzed the amount of surface deformation caused by the mirror deflection in different observation angles. Figure 13 shows the

pointing directions of the OTA and the corresponding surface deformations of the M1 and M2. Figures 13(a)–(c) show the mirror deflections when the OTA directs at 90° , 45° , and 0° in the elevation angle, respectively. Table 7 shows the amounts of decenter and rotation of the M1 and M2 assembly in these observation angles. In the horizontal direction, the y-decenter and x-rotation of the M2 are $-70.6\ \mu\text{m}$ and $0.53\ \text{arcsec}$, respectively. The z-decenter is $-44.0\ \mu\text{m}$ in the vertical direction, and the x-rotation is negligible. In the observation angle of 45° , the y-decenter, z-decenter, and x-rotation are $-49.8\ \mu\text{m}$, $-31.1\ \mu\text{m}$, and $0.25\ \text{arcsec}$, respectively. For the M1, the y-decenter and x-rotation of the M2 are $-122.1\ \mu\text{m}$ and $6.48\ \text{arcsec}$ in the horizontal direction. The z-decenter and x-rotation are $-95.4\ \mu\text{m}$ and $0.36\ \text{arcsec}$. In the observation angle of 45° , the y-decenter, z-decenter, and x-rotation are $-83.5\ \mu\text{m}$, $-66.3\ \mu\text{m}$, and $3.67\ \text{arcsec}$, respectively. These values will be used for a lookup table, and the positioning of the M2 will be implemented during its operation.

7. Fabrication and assembly process of the secondary mirror assembly

Lastly, we conducted the mirror processing and assembling for the components of the M2 assembly based on our optimized design. Figure 14(a) shows the process for realizing the lightweight of the M2 by using a T-shaped milling tool. Figures 14(b) and (c) show the mirror shapes after achieving the lightweight M2 and after the surface coating, respectively. It has a parabolic shape, and its surface quality was tested with non-contact 3D optical profilers. The SFE-z after the

Table 7. Decenter and rotation values of the M2 and M1 in the observation angles of 0° , 45° , and 90° .

| Observation angle in elevation | M2 decenter (Direction) | M2 rotation (Direction) | M1 decenter (Direction) | M1 rotation (Direction) |
|-----------------------------------|--|----------------------------|--|----------------------------|
| 0° | $-70.6\ \mu\text{m}$ (y) | $0.53\ \text{arcsec}$ (x) | $-122.1\ \mu\text{m}$ (y) | $6.48\ \text{arcsec}$ (x) |
| 45° | $-49.8\ \mu\text{m}$ (y) $-31.1\ \mu\text{m}$ (z) | $0.25\ \text{arcsec}$ (x) | $-83.5\ \mu\text{m}$ (y) $-66.3\ \mu\text{m}$ (z) | $3.67\ \text{arcsec}$ (x) |
| 90° | $-44.0\ \mu\text{m}$ (z) | negligible | $-95.4\ \mu\text{m}$ (z) | $0.36\ \text{arcsec}$ (x) |

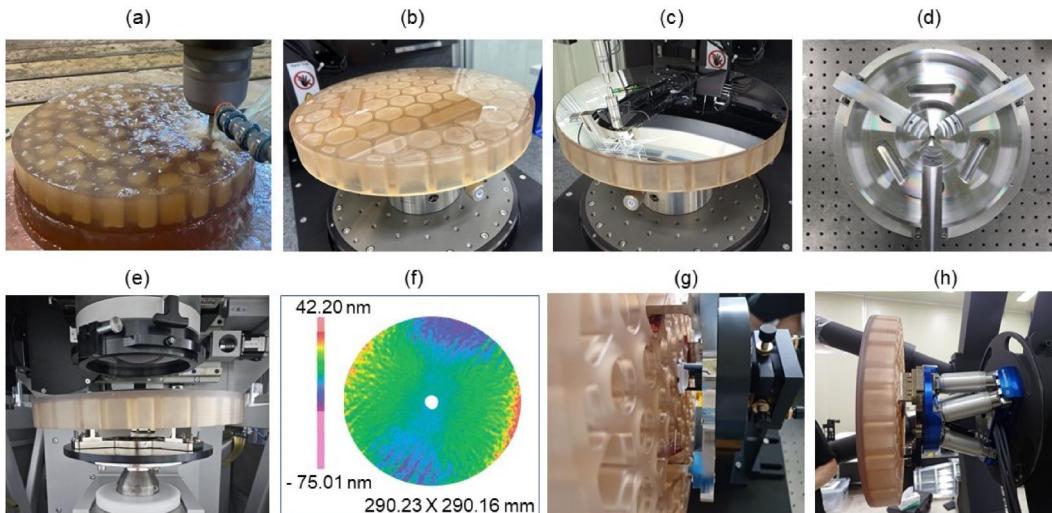


Figure 14. Fabrication and assembly procedures of the secondary mirror (M2). (a) Grinding of the lightweight mirror, (b) The lightweight M2 after the polishing, (c) The M2 after surface coating, (d) The assembling fixtures, consisting of the base and guiding fixtures, (e) Surface quality test by using Aspheric Stitching Interferometer (ASI) of QED TechnologiesTM. (f) The result for the surface measurement, (g) Aligning the flat mirror on the back of the M2, (h) M2 assembly installed on the OTA.

mirror coating was 4.2 nm of the RMS value. Figure 14(d) shows the assembled fixture, and the target accuracy for the aligning and bonding process is 100 μm . In the aligning process, we put the M2 on the base fixture and glued the flexure mounts using the guiding fixture. Here, the distances of the flexure mounts from the M2 center and their parallelisms in the axial and radial directions are important to reduce mirror deflection and bond stress. We monitored them by using a coordinate measuring machine during the alignment process. As shown in Figure 14(e), the surface quality of the M2 is tested by using an aspheric stitching interferometer (ASI) of QED TechnologiesTM. As shown in Figure 14(f), wavefront error is 12.27 nm of the RMS value. Using a spacer, we attached the flexure mounts to the designated positions. Then, we attached a flat mirror on the back of the M2 shown in Figure 14(g). The flat mirror acts as a reference plane when aligning the coude pass. We used a tip-tilt stage to position the flat mirror, making its surface parallel with the M2 surface. During the bonding process, we monitored its SFE with a Fizeau interferometer. The bonding process and the results for the surface quality test are presented in the [supplementary section](#) in detail (Figure S2). After connecting the adapter plate with the hexapod, we fastened the M2 assembly to the spider vane of the OTA with bolts. Figure 14(h) shows the installed M2 assembly on the OTA. After assembling all the components of the OTA, including the mirrors and frames, we aligned the M1, M2, and M3 assemblies. The positions of the M1 surface and M2 surface were measured with a laser tracker, and the hexapod controls the position of the M2 assembly. Finally, we controlled the piston and tilt of the M3 assembly for proper beam transfer. The total SFE-y of the mirrors was tested for the horizontal pointing direction with a Fizeau interferometer. Based on the sub-aperture stitching algorithm,^[40] the calculated total SFE-y was 27.1 nm, satisfying the SFE budget.

8. Conclusions

This study proposed an optimal design for the secondary mirror (M2) assembly in a 1-m class ground telescope. Our telescope performs both astronomical imaging and satellite laser ranging. In a ground telescope, mirror deflection is mainly induced by self-gravity and temperature change. Its gravity vector changes depending on the pointing direction of the optical tube assembly (OTA). Therefore, we designed the M2 assembly considering its deflection in different observation angles. In addition, we created a lightweight mirror based on a hexagonal structure with a partially open-back scheme. Moreover, we used flexure mounts to reduce the surface errors (SFEs) in both the horizontal and vertical pointing directions. The optimized design provides SFEs of 4.21, 2.16, and 0.28 nm in the vertical and horizontal directions, and temperature changes of 5 K, satisfying the SFE budgets. We fabricated and processed the M2 based on the optimized design and assembled it with the flexure mounts using the aligning fixtures. After assembling it, we positioned a flat mirror on the back of the M2 to provide a reference plane for the coude pass. Finally, we put the M2 assembly on the OTA frame and aligned the M1, M2, and M3 assemblies. The total SFE-y of the mirrors is 27.1 nm, measured in the horizontal pointing direction with a Fizeau interferometer. The alignment process and its results for the mirrors will be discussed in future work in detail.

Disclosure statement

The authors declare no conflicts of interest.

Funding

This work was supported by Defense Rapid Acquisition Technology Research Institute (DRATRI) – Grant funded by Defense Acquisition Program Administration (DAPA) (UC200012D).

ORCID

Jaehyun Lee  <http://orcid.org/0000-0001-5456-124X>
 Pilseong Kang  <http://orcid.org/0000-0002-2618-9249>
 Hyug-Gyo Rhee  <http://orcid.org/0000-0003-3614-5909>

References

- [1] Hill, J. M. The large binocular telescope. *Appl. Opt.* **2010**, 49, 115–122. DOI: [10.1364/AO.49.00D115](https://doi.org/10.1364/AO.49.00D115).
- [2] Johns, M. Giant Magellan telescope – Overview. *Proc. SPIE* **2013**, 4, 8444.
- [3] Madec, P.-Y. 2012 Overview of deformable mirror technologies for adaptive optics and astronomy. *Adaptive Opt. Systems* 8447. DOI: [10.1117/12.924892](https://doi.org/10.1117/12.924892).
- [4] Rausch, P.; Verpoort, S.; Wittrock, U. Unimorph deformable mirror for space telescope: design and manufacturing. *Opt. Express*. **2015**, 23, 19469–19477. DOI: [10.1364/OE.23.019469](https://doi.org/10.1364/OE.23.019469).
- [5] Riccard, A.; Brusa, G.; Salinari, P.; Gallieni, D.; Biasi, R.; Andrighettoni, M.; Martin, H. M. Adaptive secondary mirrors for the large binocular telescope. *Proc. SPIE* **2016**, 5169, 159–168.
- [6] Bouchez, A. H.; Acton, D. S.; Agapito, G.; Arcidiacono, C.; Bennet, F.; Biliotti, V.; Bonaglia, M.; Briguglio, R.; Brusa-Zappellini, G.; Busoni, L. The giant Magellan telescope adaptive optics program. *Adaptive Opt. Syst.* **2012**, 8447, 844711–844711-12. DOI: [10.1117/12.926691](https://doi.org/10.1117/12.926691).
- [7] Yoder, P. R. *Opto-Mechanical Systems Design*. (3rd ed.). Taylor & Francis: Boca Raton, 2006.
- [8] Ahmad, A. *Handbook of Optomechanical Engineering*. (2nd ed.). CRC Press: Boca Raton, FL, 1996.
- [9] Barnes, W. P. Hexagonal vs triangular core lightweight mirror structures. *Appl. Opt.* **1972**, 11, 2748–2751. DOI: [10.1364/AO.11.002748](https://doi.org/10.1364/AO.11.002748).
- [10] Chin, D. Optical mirror-mount design and philosophy. *Appl. Opt.* **1964**, 3, 895–901. DOI: [10.1364/AO.3.000895](https://doi.org/10.1364/AO.3.000895).
- [11] Park, K.-S.; Lee, J. H.; Youn, S.-K. Lightweight mirror design method using topology optimization. *Opt. Eng.* **2005**, 44, 053002. DOI: [10.1117/1.1901685](https://doi.org/10.1117/1.1901685).
- [12] Kihm, H.; Yang, H.-S. Design optimization of a 1-m lightweight mirror for a space telescope. *Opt. Eng.* **2013**, 52, 091806. DOI: [10.1117/1.OE.52.9.091806](https://doi.org/10.1117/1.OE.52.9.091806).
- [13] Jiang, P.; Zhou, P. Optimization of a lightweight mirror with reduced sensitivity to the mount location. *Appl. Opt.* **2020**, 59, 3799–3805. DOI: [10.1364/AO.383391](https://doi.org/10.1364/AO.383391).
- [14] Kihm, H.; Yang, H.-S.; Moon, I. K.; Yeon, J. H.; Lee, S.-H.; Lee, Y.-W. Adjustable bipod flexures for mounting mirrors in a space telescope. *Appl. Opt.* **2012**, 51, 7776–7783. DOI: [10.1364/AO.51.007776](https://doi.org/10.1364/AO.51.007776).
- [15] Zhang, L.; Wang, T.; Zhang, F.; Zhao, H.; Zhao, Y.; Zheng, X. Design and optimization of integrated flexure mounts for unloading lateral gravity of a lightweight mirror for space application. *Appl. Opt.* **2021**, 60, 417–426. DOI: [10.1364/AO.414054](https://doi.org/10.1364/AO.414054).
- [16] Chen, Y.-C.; Huang, B.-K.; You, Z.-T.; Chan, C.-Y.; Huang, T.-M. Optimization of lightweight structure and supporting bipod flexure for a space mirror. *Appl. Opt.* **2016**, 55, 10382–10391. DOI: [10.1364/AO.55.010382](https://doi.org/10.1364/AO.55.010382).
- [17] Ebizuka, N.; Dai, Y.; Eto, H.; Lin, W.; Ebisuzaki, T.; Omori, H.; Handa, T.; Takami, H.; Takahashi, Y. Development of SiC ultra light mirror for large space telescope and for extremely huge ground based telescope. *Proceeding of SPIE* 4842, 2003. DOI: [10.1117/12.457408](https://doi.org/10.1117/12.457408).
- [18] Liu, S.; Hu, R.; Li, Q.; Zhou, P.; Dong, Z.; Kang, R. Topology optimization-based lightweight primary mirror design of a large-aperture space telescope. *Appl. Opt.* **2014**, 53, 8318–8325. DOI: [10.1364/AO.53.008318](https://doi.org/10.1364/AO.53.008318).
- [19] Karci, O.; Ekinci, M. Design of a high-precision, 0.5 m aperture Cassegrain collimator. *Appl. Opt.* **2020**, 59, 8434–8441. DOI: [10.1364/AO.395673](https://doi.org/10.1364/AO.395673).
- [20] Cho, M.; Corredor, A.; Dribusch, C.; Park, W.H.; Muller, G.; Johns, M.; Hull, C.; Sheehan, M.; Kern, J.; Kim, Y.S.; Hansen, E. Development of the fast steering secondary mirror for the giant Magellan Telescope. *Proc. SPIE*. 8836. 2013. DOI: [10.1117/12.2024164](https://doi.org/10.1117/12.2024164).
- [21] Zhang, Y.; Jiang, H.; Shectman, S.; Yang, D.; Cai, Z.; Shi, Y.; Huang, S.; Lu, L.; Zheng, Y.; Kang, S.; Mao, S. Conceptual design of the optical system of the 6.5 m wide field multiplexed survey telescope with excellent image quality. *PhotonIX* **2023**, 4, 16. DOI: [10.1186/s43074-023-00094-4](https://doi.org/10.1186/s43074-023-00094-4).
- [22] Snyder, G. L.; Hurst, S. R.; Grafinger, A. B.; Halsey, H. W. Satellite laser ranging experiment. *Proc. IEEE* **1965**, 53, 298–299. DOI: [10.1109/PROC.1965.3691](https://doi.org/10.1109/PROC.1965.3691).
- [23] Samain, E.; Phung, D. H.; Maurice, N.; Albanese, D.; Mariey, H.; Aimar, M.; Lagarde, G. M.; Vedrenne, N.; Velluet, M. T.; Artaud, G.; Issler, J.L. First free space optical communication in Europe between SOTA and MeO optical ground station. In 2015 IEEE International Conference on Space Optical Systems and Applications (ICSOS), IEEE, 2015.
- [24] Gurtner, W.; Noomen, R.; Pearlman, M. R. The international laser ranging service: current status and future developments. *Adv. Space Res.* **2005**, 36, 327–332. DOI: [10.1016/j.asr.2004.12.012](https://doi.org/10.1016/j.asr.2004.12.012).

- [25] Wilkinson, M.; Schreiber, U.; Procházka, I.; Moore, C.; Degnan, J.; Kirchner, G.; Zhongping, Z.; Dunn, P.; Shargorodskiy, V.; Sadovnikov, M.; et al. The next generation of satellite laser ranging systems. *J. Geod.* **2019**, *93*, 2227–2247. DOI: [10.1007/s00190-018-1196-1](https://doi.org/10.1007/s00190-018-1196-1).
- [26] McGarry, J. F.; Hoffman, E. D.; Degnan, J. J.; Cheek, J. W.; Clarke, C. B.; Diegel, I. F.; Donovan, H. L.; Horvath, J. E.; Marzouk, M.; Nelson, A. R.; Patterson, D. S. NASA's satellite laser ranging systems for the 21st century. *J. Geod.* **2018**, *93*, 1–15.
- [27] Toyoshima, M.; Takayama, Y.; Takahashi, T.; Suzuki, K.; Kimura, S.; Takizawa, K.; Kuri, T.; Klaus, W.; Toyoda, M.; Kunimori, H.; Jono, T. Ground-to-satellite laser communications experiments. *IEEE A&E Syst. Mag.* **2008**, *23*, 10–18.
- [28] Kaushal, H.; Kaddoum, G. Optical communication in space: challenges and mitigation techniques. *IEEE Commun. Surv. Tutor* **2016**, *19*, 57–96. DOI: [10.1109/COMST.2016.2603518](https://doi.org/10.1109/COMST.2016.2603518).
- [29] Ciufolini, I.; Paolozzi, A.; Pavlis, E. C.; Ries, J.; Koenig, R.; Matzner, R.; Sindoni, G.; Neumayer, H. Testing gravitational physics with satellite laser ranging. *Eur. Phys. J. Plus.* **2011**, *126*, 1–9. DOI: [10.1140/epjp/i2011-11072-2](https://doi.org/10.1140/epjp/i2011-11072-2).
- [30] Kucharski, D.; Kirchner, G.; Koidl, F.; Carman, R.; Moore, C.; Dmytrotso, A.; Ploner, M.; Bianco, G.; Medvedskij, M.; Makeyev, A. Attitude and spin period of space debris envisat measured by satellite laser ranging. *IEEE Trans. Geosci. Remote Sens.* **2014**, *52*(12), 7651–7657. DOI: [10.1109/TGRS.2014.2316138](https://doi.org/10.1109/TGRS.2014.2316138).
- [31] Steindorfer, M. A.; Kirchner, G.; Koidl, F.; Wang, P.; Jilete, B.; Flohrer, T. Daylight space debris laser ranging. *Nature Comm.* **2020**, *11*, 1–6.
- [32] Varghese, T. K.; Decker, W. M.; Crooks, H. A.; Bianco, G. Matera laser ranging observatory (MLRO): An overview. In Proc. Eighth International Workshop on Laser Ranging Instrumentation (NASA, Goddard space flight center, USA, Jun. 1, 1993).
- [33] Samain, E.; Phung, D. H.; Maurice, N.; Albanese, D.; Mariey, H.; Aimar, M.; Lagarde, G. M.; Vedrenne, N.; Velluet, M. T.; Artaud, G.; Issler, J. L. First free space optical communication in Europe between SOTA and MeO optical ground station. In Proc. 2015 IEEE International Conference on Space Optical Systems and Applications (New Orleans, LA, USA, Oct. 26–28, 2015), 1–7.
- [34] Kim, D.-W.; Park, S. Y.; Rhee, H. G.; Kang, P. Mechanical design for an optical-telescope assembly of a satellite-laser-ranging system. *Curr. Opt. Photon.* **2023**, *7*, 419–427.
- [35] Lee, J.; Rhee, H. G.; Son, E. S.; Kang, J. G.; Jeong, J. Y.; Kang, P. Optimal design of a Coudé mirror assembly for a 1-m class ground telescope. *Curr. Opt. Photon.* **2023**, *7*, 435–442.
- [36] <https://symetrie.fr/en/hexapods/bora/>.
- [37] Kang, P.; Huh, J.; Lee, K.; Park, S.; Rhee, H.-G. Design of a discrete flexure for a SiC deformable mirror with PMN stacked-actuators. *Opt. Express.* **2021**, *29*, 31778–31795. DOI: [10.1364/OE.436362](https://doi.org/10.1364/OE.436362).
- [38] Niu, K.; Tian, C. Zernike polynomials and their applications. *J. Opt.* **2022**, *24*, 123001. DOI: [10.1088/2040-8986/ac9e08](https://doi.org/10.1088/2040-8986/ac9e08).
- [39] International Organization for Standardization (ISO). Optics and photonics—interferometric measurement of optical elements and optical systems—Part 2: measurement and evaluation techniques. 2005.
- [40] Seo, Y. B.; Joo, K.-N.; Ghim, Y.-S.; Rhee, H.-G. Subaperture stitching wavelength scanning interferometry for 3D surface measurement of complex-shaped optics. *Meas. Sci. Technol.* **2021**, *32*, 045201. DOI: [10.1088/1361-6501/abd056](https://doi.org/10.1088/1361-6501/abd056).